ADVANCED FUNCTIONAL MATERIALS
www.afm-journal.de

Ultrahigh Specific Capacitances for Supercapacitors Achieved by Nickel Cobaltite/Carbon Aerogel Composites

*Hsing-Chi Chien, Wei-Yun Cheng, Yong-Hui Wang, and Shih-Yuan Lu**

Nickel cobaltite, a low cost and an environmentally friendly supercapacitive material, is deposited as a thin nanostructure of 3–5 nm nanocrystals into carbon aerogels, a mesoporous host template of high specific surface areas and high electric conductivities, with a two-step wet chemistry process. This nickel cobaltite/carbon aerogel composite shows ultrahigh specific capacitances of around 1700 F g^{-1} at a scan rate of 25 mV s^{-1} within a potential window of −0.05 to 0.5 V in 1 M NaOH solutions. The composite also possesses an excellent high rate capability manifested by maintaining specific capacitances above 800 F g^{-1} at a high scan rate of 500 mV s^{-1}, and an outstanding cycling stability demonstrated by a negligible 2.4% decay in specific capacitances after 2000 cycles. The success is attributable to the fuller utilization of nickel cobaltite for pseudocapacitance generation, made possible by the composite structure enabling well exposed nickel cobaltite to the electrolyte and easy transport of charge carriers, ions, and electrons, within the composite electrode.

1. Introduction

Energy storage devices are an essential part of the clean energy era necessary to tackle the ever worsening fossil energy depletion and global warming issues. Among the many presently existing energy storage devices, lithium ion batteries and supercapacitors are considered by many the two most important ones. Supercapacitors, when compared with lithium ion batteries, possess much longer cycle life, much higher power densities, and much shorter charging/discharging times, but much lower energy densities.[1] One of the key issues in supercapacitor development is thus to boost the energy density to be more comparable with those of lithium ion batteries. Both energy density and power density are directly proportional to the specific capacitances of the supercapacitors. Consequently, intensive and extensive research efforts have been directed to the improvement of specific capacitances.[2–4]

The magnitudes of specific capacitances mainly depend on the capacitive properties and microstructure of the electrode materials. For the time being, hydrous RuO_2 is considered the most prominent electrode material for supercapacitors, with an ultrahigh specific capacitance of 1580 F g^{-1} (measured at 1 mV s^{-1}) reported in the literature.[2] Its commercialization however is not promising because of the high cost and rareness of Ru. On the contrary, spinel nickel cobaltite ($NiCo_2O_4$) is a low-cost, environmentally friendly transition metal oxide, with both its constituent elements being relatively Earth-abundant, possessing also excellent capacitive properties.[4] In fact, it has been demonstrated to exhibit an outstanding specific capacitance of 1400 F g^{-1} (measured at 25 mV s^{-1}) when prepared in an aerogel form.[4] Nickel cobaltite was also synthesized as hierarchical porous nanowires[5] and grown as nanoparticles on graphene sheets[6] in an attempt to improve the capacitive performances of nickel cobaltite through novel nanostructure design. The specific capacitance performances of the porous $NiCo_2O_4$ nanowires and $NiCo_2O_4$/graphene composites however were not able to exceed those of nickel cobaltite aerogels. Aerogels are a class of mesoporous materials possessing high specific surface areas, high porosities, and three-dimensionally well-connected through pore structure. These structural features favor aerogels for applications involving heterogeneous reactions at solid-liquid interfaces such as electrodes and catalysts.[3,4,7–9] For the heterogeneous processes to proceed efficiently, large surface areas to provide abundant active sites for the interfacial events, high porosities and through pore structure to enable fast mass transfer of the liquid species to access the active sites, and 3D well-connected network to offer continuous charge transport passageways, are desirable.

Although great success has been achieved with $NiCo_2O_4$ aerogels for supercapacitor applications, significant improvements are still possible by further enhancing the specific surface area and electric conductivity of the electrode together with better utilization of $NiCo_2O_4$. This goal can be achieved by using a mesoporous matrix of high electric conductivities and high specific surface areas to host $NiCo_2O_4$, the active material,[10–16] with $NiCo_2O_4$ deposited as a thin nanostructure onto the backbone of the mesoporous matrix to enable a fuller utilization of $NiCo_2O_4$ for capacitance generations.[7,12,16] The idea is to expose the active material as much as possible to the electrolyte so that the capacitance generation through superficial redox reactions can proceed to a fuller extent. The superficial redox reactions further require a fast mass transfer of the electrolyte in and out of the mesoporous structure. A rapid charge transport within the active material domain is also beneficial. Both scenarios can be realized with the present composite design. The thin

H.-C. Chien, W.-Y. Cheng, Y.-H. Wang, Prof. S.-Y. Lu
Department of Chemical Engineering
National Tsing-Hua University
Hsin-Chu, Taiwan 30013, Republic of China
E-mail: SYLU@mx.nthu.edu.tw

DOI: 10.1002/adfm.201201176

nanostructure of the active material enables exposition of its large surface areas to the electrolyte and shortens the travel distance for the charge transport within the much less conductive active material domain. The highly porous and 3D well-connected through pore structure of the matrix makes possible the fast mass transfer of the electrolyte.

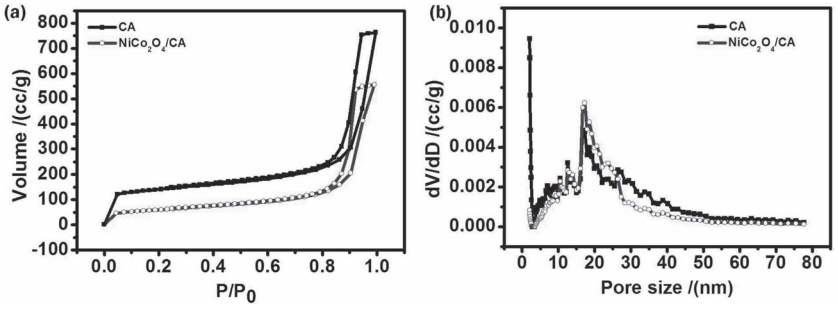

Figure 2. a) N_2 adsorption/desorption isotherms and b) pore size distributions of carbon aerogel and $NiCo_2O_4$/carbon aerogel composite.

2. Results and Discussion

In this work, $NiCo_2O_4$ is introduced into a highly conductive, mesoporous carbon aerogel (CA)[17] matrix in a form of uniformly distributed nanocrystals of 3–5 nm in size to serve as the supercapacitor electrode. Note here the specific surface area and electric conductivity of carbon aerogels are much higher than those of $NiCo_2O_4$ aerogels, and can thus further enhance the utilization of $NiCo_2O_4$ to achieve even higher specific capacitances. The CA matrix is found to contribute negligible capacitances to the composite, and thus its role may be viewed as an extended substrate, only that this extended substrate is highly porous.

To obtain a conformal coating of the thin nanostructure of the active material onto the backbone of the mesoporous matrix however is not a trivial task. Here, we develop a two-step wet chemistry process for the conformal thin nanostructure formation. The precursors of the active material are first introduced to coat on the backbone of the porous matrix, followed by introduction of the reaction initiator to trigger the nanocrystal formation reaction. This design ensures the formation of the active material on the backbone of the matrix instead of in the bulk of the reacting solution. Note that products from bulk reactions may not deposit as a conformal thin nanostructure onto the backbone of the porous matrix. The present approach differs from the more commonly adopted process, i.e., formation of the active material sols first followed by immersion of the matrix into the sol solution to afford the composite.[18–21]

Figure 1 shows the XRD pattern of the $NiCo_2O_4$/CA composite. Also included in Figure 1 are the diffraction patterns of the CA and $NiCo_2O_4$ aerogel for comparison. Two broad peaks can be identified for the CA and they also appear in the diffraction pattern of the $NiCo_2O_4$/CA composite. As for the $NiCo_2O_4$ aerogel, the diffraction pattern matches well with that of $NiCo_2O_4$ of the normal spinel phase (JCPDS # 73–1704), with the three most pronounced peaks indexed to the (111), (311), and (400) diffractions. Again, these three peaks can be identified in the diffraction pattern of the $NiCo_2O_4$/CA composite. From the comparison, it is evident that the diffraction pattern of the $NiCo_2O_4$/CA composite contains diffraction peaks contributed from both the CA and $NiCo_2O_4$ aerogel, thus confirming not only the successful incorporation of $NiCo_2O_4$ into the CA, but also the crystalline phase of the incorporated $NiCo_2O_4$ to be the normal spinel phase.

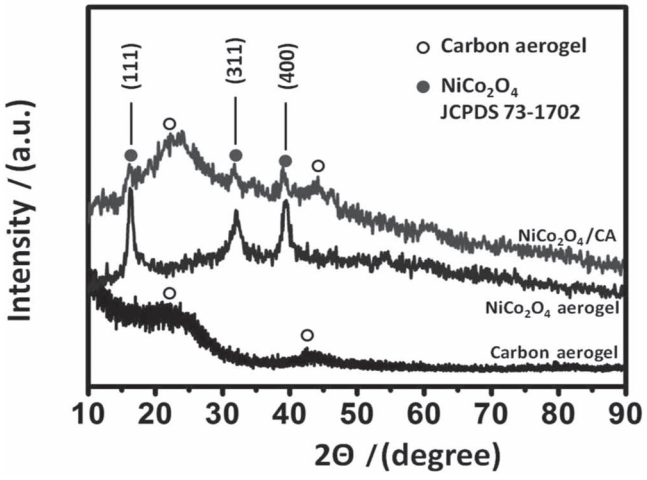

Figure 1. XRD patterns of carbon aerogel, $NiCo_2O_4$ aerogel, and $NiCo_2O_4$/carbon aerogel composite.

Figure 2a shows the N_2 adsorption/desorption isotherms of the CA and $NiCo_2O_4$/CA composite. Both isotherms exhibit the characteristics of type IV isotherms with a pronounced type H1 hysteresis loop, typical for mesoporous materials. The two isotherms resemble each other with the one from the composite sample located lower in adsorption volumes, implying that the incorporation of $NiCo_2O_4$ does not change the essential microstructural characteristics of the CA, but only reduces the surface area and pore space available for the N_2 adsorption. Figure 2b displays the corresponding pore size distributions of the two samples. The CA sample exhibits a bi-modal distribution with the first pore size peak located in the micropore region. These micropores however are almost completely removed after the incorporation of $NiCo_2O_4$, giving essentially a single-modal pore size distribution. The relevant structural parameters derived from the isotherms are summarized in **Table 1** and further discussed below. The specific surface area and pore volume of the CA sample are reduced from 449 and 1.07 to 206 $m^2\ g^{-1}$ and 0.818 $cm^3\ g^{-1}$, respectively after the $NiCo_2O_4$ incorporation. The micropores of the CA sample contribute 51% (231 $m^2\ g^{-1}$) of the specific surface area and 11% (0.123 $cm^3\ g^{-1}$) of the pore volume, which are greatly reduced

Table 1. Specific surface areas, pore volumes, and average pore sizes of carbon aerogel and nickel cobaltite/carbon aerogel composite

Sample	Specific surface area (from micropores) [$m^2\ g^{-1}$]	Pore volumes (from micropores) [$cm^3\ g^{-1}$]	Average pore size [nm]
CA	449 (231)	1.07 (0.123)	10.5
$NiCo_2O_4$/CA	206 (40)	0.818 (0.02)	16.7

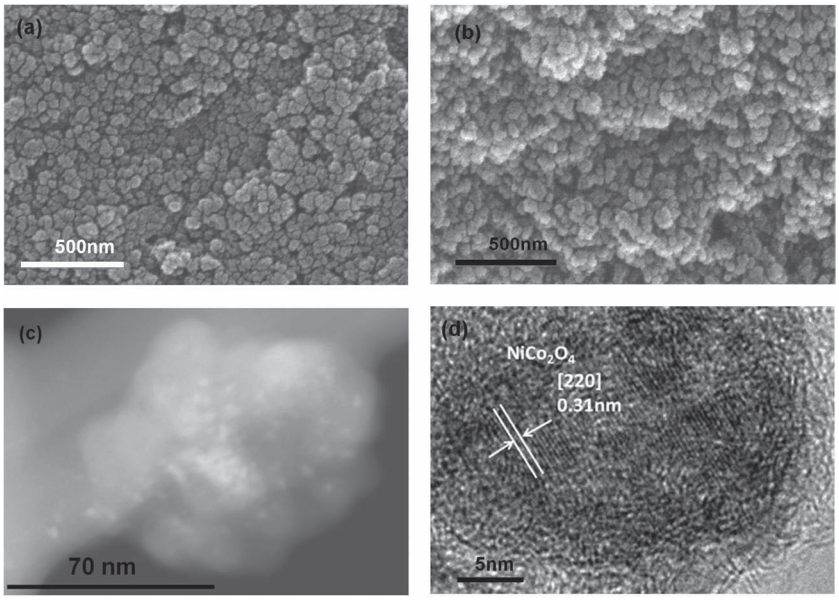

Figure 3. a,b) SEM images of carbon aerogel and $NiCo_2O_4$/carbon aerogel composite, respectively. c,d) HAADF and HRTEM images of $NiCo_2O_4$/carbon aerogel composite, respectively.

to only 19 (40 m^2 g^{-1}) and 2% (0.02 cm^3 g^{-1}), respectively for the $NiCo_2O_4$/CA sample, indicating significant filling/blocking of the micropores with the deposition of $NiCo_2O_4$. Because of the micropore removal, the average pore size increases from 10.5 to 16.7 nm. The sizes of the mesopores however decrease because of the $NiCo_2O_4$ incorporation as evident from the left shift of the pore size distribution at the larger pore size side shown in Figure 2b. Note that the slight left shift in the pore size distribution implies also a successful conformal thin coating of the incorporated $NiCo_2O_4$ on the backbone of the carbon aerogel. If the coating is not conformal and thin, then the pore structure of the carbon aerogel will be altered to a greater extent, thus leading to a much left-shifted and possibly shape-changed pore size distribution. The conformal thin coating of the incorporated material is a key for the success of the present design. A conformal and thin coating of $NiCo_2O_4$ not only favors the fuller extent of exposition of $NiCo_2O_4$ to the electrolyte, but also retains the original advantageous structural features of the host matrix as being highly porous and possessing high specific surface areas.

Figure 3a,b show the SEM images of the fractured CA and $NiCo_2O_4$/CA samples. No apparent differences can be observed from the two figures. This is consistent with the N_2 adsorption/desorption data in that the introduction of $NiCo_2O_4$ does not change the essential microstructural characteristics of the CA sample. Figure 3c shows a high-angle annular dark-field (HAADF) image of the composite sample, which appears as a clump of about 110 nm in size obtained from the fractured monolithic $NiCo_2O_4$/CA composite. One can observe many bright spots distribute quite uniformly on this clump. These bright spots are with a size of 3–5 nm and can be identified as the $NiCo_2O_4$ domain. Note that the atomic numbers (Z) of Ni and Co are significantly larger than that of C and the signal intensity of the HAADF imaging is proportional to Z^2 of the elements. Consequently, these much brighter spots must be contributed by the deposited $NiCo_2O_4$ nanocrystals. Figure 3d shows an HRTEM image of the composite sample. Several nanocrystals are observed to sit on top of an object. These nanocrystals are with a size of 3–5 nm, consistent with the observation of the HAADF image. The interlayer spacing of 0.31 nm agrees well with the *d*-spacing of the normal spinel $NiCo_2O_4$ in the [220] direction. The HAADF and HRTEM images, in addition to the XRD patterns, confirm the successful incorporation of $NiCo_2O_4$ into the CA matrix. Note that the observed samples are grinded products from monolithic $NiCo_2O_4$/CA composites. Therefore, the images obtained from the HAADF detector or HRTEM show the inner microstructure of the composite instead of the surface microstructure of the monolithic sample. From the information revealed in Figure 3, it can be concluded that $NiCo_2O_4$ is successfully introduced into the CA matrix in a form of nanocrystals uniformly distributed on the backbone of the CA matrix. This is highly desirable for the fuller utilization of $NiCo_2O_4$ for superficial redox reactions to generate capacitances since the thin nanostructure of $NiCo_2O_4$ is well exposed to the electrolyte and the charge travel distance within the $NiCo_2O_4$ domain is short.

The capacitive characteristics of the $NiCo_2O_4$/CA composite are investigated with cyclic voltammetric measurements and constant current charging/discharging. **Figure 4**a shows the cyclic voltammogram (CV) of the $NiCo_2O_4$/CA composite at the 300th cycle with a scan rate of 25 mV s^{-1}, an electrolyte of 1 M NaOH, and a potential window of –0.1–0.55 V vs. Ag/AgCl. Also included for comparison are the CVs of the CA and $NiCo_2O_4$ aerogel. Here, each sample electrode is constructed with a 1 × 1 cm^2 working area and the vertical axis of the plot is in area-based current density to give a direct comparison in total currents generated by the electrode. Evidently, the currents generated by the CA matrix are negligible as compared with those of the other two samples so that the contribution to the capacitances made by the CA matrix is safely neglected in the specific capacitance data reported here. It has been found that carbon aerogels performed poorly in terms of capacitance generations when the electrolyte is neutral[7] or moderately alkaline (e.g., 1.0 M NaOH used in the present work). Their capacitive performances however improve significantly when highly alkaline (e.g., 5 M KOH)[22,23] or moderately acidic (e.g., 0.5 M H_2SO_4) electrolytes are used. The CA matrix here serves more like a highly porous extended substrate for the active material.

The CVs of the $NiCo_2O_4$/CA and $NiCo_2O_4$ aerogel samples resemble each other as they should, but with the currents generated at the low potential region remaining finite for the $NiCo_2O_4$/CA sample, instead of close to zero for the $NiCo_2O_4$ aerogel sample. This indicates a wider effective working potential window for the $NiCo_2O_4$/CA composite, probably resulting from the improvement in $NiCo_2O_4$ utilization and overall charge transport made possible by the use

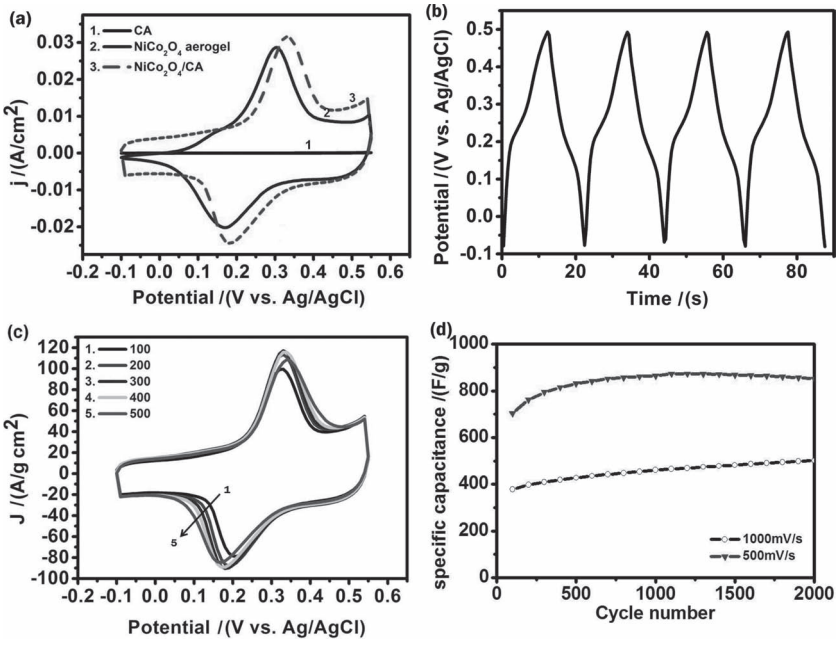

Figure 4. a) Cyclic voltammograms of carbon aerogel, $NiCo_2O_4$ aerogel, and $NiCo_2O_4$/carbon aerogel composite. b) Charging/discharging cycles of $NiCo_2O_4$/carbon aerogel composite. c) Cyclic voltammograms of $NiCo_2O_4$/carbon aerogel composites at cycles 100, 200, 300, 400, and 500. d) Cyclic stabilities of $NiCo_2O_4$/carbon aerogel composites at 500 and 1000 mV/s.

of the CA matrix to accommodate $NiCo_2O_4$. Note that transition metal oxides offer not only pseudocapacitances generated from relevant Faradaic redox reactions but also electric double layer capacitances from their surfaces exposed to the electrolyte. The flat portions observed at the lower potential region of the CV of the $NiCo_2O_4$/CA composite may be a combined effect of the two types of capacitances. This type of phenomenon is however not uncommon for transition metal oxides, for example, manganese oxide.[7,11,12] The linear depenence of current density versus scan rate expected for both pseudocapacitances and electric double layer capacitances is checked satisfactory.[24] Because of this improvement in CV performance, a boost in specific capacitances for the $NiCo_2O_4$/CA composite over that of the $NiCo_2O_4$ aerogel is expected. In fact, the specific capacitance calculated from the present CV is 1695 F g^{-1} for the $NiCo_2O_4$/CA composite based on a potential window of –0.05 to 0.5 V, almost 300 F g^{-1} higher than the maximum value of 1400 F g^{-1} achieved for the $NiCo_2O_4$ aerogel at the 500th cycle based on a potential window of 0.04–0.52 V,[4] proving the advantage of using CA as the host template for the active material, $NiCo_2O_4$. For ultrahigh specific capacitances, an improvement of 21% (from 1400 to 1695 F g^{-1}) is considered significant.

Figure 4b shows the constant current charging/discharging plot of the $NiCo_2O_4$/CA composite at a current density of 10 mA cm^{-2} in 1 M NaOH operated in the potential window of –0.1–0.5V. The charging and discharging curves are quite symmetric, implying good cycling efficiency, defined as the ratio of the discharged energy to the charged energy at each charging/discharging cycle. The cycling efficiencies are maintained above 90% for the first 1000 cycles (data not shown). In addition, no appreciable internal electric resistances (IR drops) are observed from the curves, indicating the success in using the conductive carbon aerogel as the matrix and the thinness of the $NiCo_2O_4$ nanostructure deposited on the backbone of the CA matrix. The specific capacitances determined from the present constant current charging/discharging plot reach a maximum of 1455 F g^{-1} at cycle 600, in reasonable agreement with that computed from the CV data. It is to be stressed that the specific capacitance value depends on the constant current density imposed for the charging/discharging plot just as the specific capacitance value varies with the scan rate used for the CV loops. Higher current densities or scan rates give lower specific capacitances because of the increasing dominance of the internal resistances. Reasonably high current densities or scan rates however should be used when reporting specific capacitance values in order to have results that are practically meaningful. Here, we use the specific capacitance values obtained from the CV loops based on a scan rate of at least 25 mV s^{-1} for a practical and consistent comparison with previously reported data.

Figure 4c shows the CV loops for cycles 100, 200, 300, 400, and 500. The loop shape and enclosed areas remain roughly unchanged, an indication of excellent cycling stability. The specific capacitances increase from 1450, 1636, 1695 to 1696 F g^{-1} with increasing cycle number from 100 to 400, and then decrease slightly to 1659 F g^{-1} at cycle 500. Here, the initial increase in specific capacitances is caused by the so-called electrochemical activation phenomenon commonly encountered in electrochemical processes.[25] The volumetric capacitance corresponding to the maximum gravimetric capacitance of 1696 F g^{-1} is 110 F cm^{-3}, a reasonably high value for highly porous matrix based composite supercapacitor electrodes.[12] Figure 4d shows the specific capacitances versus cycle number for the $NiCo_2O_4$/CA composite at high scan rates of 500 and 1000 mV s^{-1}. The specific capacitances are maintained at around 800 F g^{-1} even at the high scan rate of 500 mV s^{-1}, indicating the excellent high rate capability of the electrode. With a 20 fold increase in scan rate (from 25 to 500 mV s^{-1}), the specific capacitances drop only about 50% as compared with those obtained at 25 mV s^{-1}. Furthermore, the electrochemical activation phenomenon is again observed in the first 1100 cycles, with the specific capacitance reaching a maximum of 873 F g^{-1}. The cycling stability is excellent, with the specific capacitance maintained at 852 F g^{-1} at cycle 2000, only a 2.4% drop from the maximum value. The specific caspacitances drop further to the level of around 400–500 F g^{-1} when the scan rate is increased to 1000 mV s^{-1}. At this extremely high scan rate, the cycling stability appears even better than that of the 500 mV s^{-1} case. In fact, the specific capacitances keep increasing to a value of 501 F g^{-1} at cycle 2000. This phenomenon indicates that the electrochemical activation process continues to higher cycle numbers at higher scan rates, probably because there is less time available for the activation to

penetrate into deeper active material domain and thus more cycles are needed to complete the activation, when operared at high scan rates.

3. Conclusions

An outstanding supercapacitor electrode material, $NiCo_2O_4$/CA composite, is developed, exhibiting an ultrahigh specific capacitance of around 1700 F g^{-1} at a scan rate of 25 mV s^{-1} and potential window size of 0.55 V. The success is attributed to the fuller utilization of $NiCo_2O_4$ made possible by using highly conductive mesoporous carbon aerogels as the host matrix and the successful creation of an ultrathin $NiCo_2O_4$ nanostructure on the backbone of the matrix through a two-step wet chemistry process.

4. Experimental Section

Preparation of Carbon Aerogels: Carbon aerogels are prepared with a condensation polymerization process using resorcinol and formaldehyde as the precursors.[26,27] Briefly, resorcinol (26.4 g, 98%, Acros) and sodium carbonate (0.035 g, 99%, Showa) are dissolved in de-ionized water (34.735 mL), and then added with formaldehyde (35 mL, 36.6 wt%, Cecho) to proceed with the polymerization. The reaction proceeds for 90 min to form a transparent yellowish sol. The sol is let undisturbed for one day before placing it in an oven of 50 °C for another day to form a dark brownish gel. The wet gel is aged for five days in an oven of 80 °C, followed by repeated immersion rinsing with absolute ethanol. The ethanol soaked product is dried with supercritical CO_2 (SAMDRI-795, Tousimis), and then carbonized in N_2 atmosphere at 1000 °C for 10 h to afford the carbon aerogel.

Preparation of $NiCo_2O_4$ Aerogels: For comparison purposes, $NiCo_2O_4$ aerogels are also prepared and characterized following the procedures reported previously.[4] Briefly, $NiCl_2{\cdot}6H_2O$ (0.78 mmole) and $CoCl_2{\cdot}6H_2O$ (1.56 mmole) are first dissolved in ethanol (2.5 mL), followed by addition of propylene oxide at a propylene oxide/metal ion molar ratio of 11:1. The solution is stirred for 10 min, and then let still to gel at room temperature. The wet gel is then washed with ethanol several times and dried with a supercritical dryer. The dried aerogel is further calcined at 200 °C for 5 h for use.

Preparation of $NiCo_2O_4$/CA Composite Electrodes: To prepare the $NiCo_2O_4$/CA composite, the monolithic CA is immersed in ethanolic solution (2.5 mL) of $CoCl_2{\bullet}6H_2O$ (0.74 g, 95%, Showa) and $NiCl_2{\cdot}6H_2O$ (0.37 g, 98%, Showa) for one day, followed by drying at 50 °C for another day. The dried CA is then immersed in propylene oxide (99%, Acros) for four days to proceed with the necessary hydrolysis and polycondensation reactions for formation of $NiCo_2O_4$ nanocrystals on the surfaces of the CA backbones. The product composite is obtained after rinsing with ethanol and drying with supercritical CO_2. The dried product is further calcined at 200 °C for 5 h for use. The content of $NiCo_2O_4$ in the composite is determined to be 9.2 wt% by the weight difference before and after the $NiCo_2O_4$ incorporation based on 2 grams of starting CA. The composite is grinded into fine powders and mixed with a solid binder, poly(vinylidene fluoride), at a weight ratio of 10:1. The mixture is suspended in 1-methyl-2-pyrrolidone (50 μL), a binder solvent, with ultrasound agitation for 1 h. The suspension is then drop-cast on a graphite substrate and dried at 80 °C for 12 h to afford the $NiCo_2O_4$/CA composite electrode. The amount of $NiCo_2O_4$ is controlled to be around 0.23 mg and the working area of the electrode is set at 1×1 cm^2.

Characterizations: The XRD patterns of the samples are recorded with an X-ray powder diffractometer (Cu$K\alpha$, NEW D8 ADVANCE, Bruker). The samples are ground into fine powders for the measurements at a scan rate of 6° min^{-1}. The specific surface areas, pore volumes, and average pore sizes are obtained from the N_2 adsorption/desorption isotherms conducted at 77 K (NOVA e1000, Quantachrome). The electron microscopic images are obtained with a scanning electron microscope (S-4700, Hitachi) and a high resolution transmission electron microscope (JEM-3000F, Joel). Cyclic voltammetric measurements (CHI6275D, CH Instruments Inc.) are conducted in a three-electrode system with a 1M NaOH solution serving as the electrolyte. The reference electrode and counter electrode are Ag/AgCl and platinum coil, respectively. The potential is scanned between −0.1 and 0.55 V with different scan rates (v).

The specific capacitances are calculated by two different methods, namely, CV method and constant current charging/discharging method. For the CV method, the specific capacitance is computed by using the definition formula of $C_s = Q(m\Delta V)^{-1}$, where Q is the average total charge, m is the mass of the active material, and ΔV is the scanned potential window size. The average total charge is taken as half of the enclosed area of the CV loop. As for the constant current charging/discharging method, the specific capacitance is obtained with the definition formula of $C_s = (I\Delta t)(m\Delta V)^{-1}$, where I is the discharging current, Δt is the discharging time, and ΔV is the resulting potential window size. Here, $NiCo_2O_4$ is taken as the sole active material since the CA offers only negligible contributions to the capacitance as evident from Figure 4a.

Acknowledgements

This work is financially supported by the National Science Council of the Republic of China (Taiwan) under grant NSC-98-2221-E-007-034-MY3. The authors thank Miss Hsuan-Ching Chen of our department for assistances in data presentation.

Received: April 28, 2012
Revised: July 9, 2012
Published online: July 25, 2012

[1] J. R. Miller, A. F. Burke, *ECS Interface* **2008**, *17*, 53.
[2] C.-C. Hu, W.-C. Chen, *Electrochim. Acta* **2004**, *49*, 3469.
[3] T.-Y. Wei, C.-H. Chen, K.-H. Chang, S.-Y. Lu, C.-C. Hu, *Chem. Mater.* **2009**, *21*, 3228.
[4] T.-Y. Wei, C.-H. Chen, H.-C. Chien, S.-Y. Lu, C.-C. Hu, *Adv. Mater.* **2010**, *22*, 347.
[5] H.-W. Wang, Z.-A. Hu, Y.-Q. Chang, Y.-L. Chen, H.-Y. Wu, Z.-Y. Zhang, Y.-Y. Yang, *J. Mater. Chem.* **2011**, *21*, 10504.
[6] H. Jiang, J. Ma, C. Li, *Chem. Commun.* **2012**, *48*, 4465.
[7] Y.-H. Lin, T.-Y. Wei, H.-C. Chien, S.-Y. Lu, *Adv. Energy Mater.* **2011**, *1*, 901.
[8] C.-C. Lin, T.-Y. Wei, K.-T. Lee, S.-Y. Lu, *J. Mater. Chem.* **2011**, *21*, 12668.
[9] H.-C. Chien, W.-Y. Cheng, Y.-H. Wang, T.-Y. Wei, S.-Y. Lu, *J. Mater. Chem.* **2011**, *21*, 18180.
[10] X. Zhang, W. Shi, J. Zhu, D. J. Kharistal, W. Zhao, B. S. Lalia, H. H. Hng, Q. Yan, *ACS Nano* **2010**, *4*, 4505.
[11] J. W. Long, M. B. Sassin, A. E. Fischer, D. R. Rolison, A. N. Mansour, V. S. Johnson, P. E. Stallworth, S. G. Greenbaum, *J. Phys. Chem. C.* **2009**, *113*, 17595.
[12] A. E. Fischer, K. A. Pettigrew, D. R. Rolison, R. M. Stroud, J. W. Long, *Nano Lett.* **2007**, *7*, 281.
[13] D. R. Rolison, J. W. Long, J. C. Lytle, A. E. Fischer, C. P. Rhodes, T. M. McEvoy, M. E. Bourg, A. M. Lubers, *Chem. Soc. Rev.* **2009**, *38*, 226.
[14] A. Pan, D. Liu, X. Zhou, B. B. Garcia, S. Liang, J. Liu, G. Cao, *J. Power Sources* **2010**, *195*, 3893.

[15] J. C. Lytle, J. M. Wallace, M. B. Sassin, A. J. Barrow, J. W. Long, J. L. Dysart, C. H. Renninger, M. P. Saunders, N. L. Brandell, D. R. Rolison, *Energy Environ. Sci.* **2011**, *4*, 1913.
[16] T. Bordjiba, D. Belanger, *J. Electrochem. Soc.* **2009**, *156*, A378.
[17] J. Biener, M. Stadermann, M. Suss, M. A. Worsley, M. M. Biener, K. A. Rose, T. F. Baumann, *Energy Environ. Sci.* **2011**, *4*, 656.
[18] M. A. Worsley, S. O. Kucheyev, J. D. Kuntz, T. Y. Olson, T. Y.-J. Han, A. V. Hamza, J. H. Satcher Jr., T. F. Baumann, *Chem. Mater.* **2011**, *23*, 3054.
[19] T. Y.-J. Han, M. A. Worsley, T. F. Baumann, J. H. Satcher Jr., *J. Mater. Chem.* **2011**, *21*, 330.
[20] M. A. Worsley, J. D. Kuntz, J. H. Satcher Jr., T. F. Baumann, *J. Mater. Chem.* **2010**, *20*, 4840.
[21] M. A. Worsley, J. D. Kuntz, O. Cervantes, T. Y.-J. Han, A. E. Gash, J. H. Satcher Jr., T. F. Baumann, *J. Mater. Chem.* **2009**, *19*, 7146.
[22] J. Li, X. Y. Wang, Q. H. Huang, S. Gamboa, P. J. Sebastian, *J. Power Sources* **2006**, *158*, 784.
[23] T. Bordjiba, M. Mohamedi, L. H. Dao, *Adv. Mater.* **2008**, *20*, 815.
[24] B. E. Conway, V. Birss, J. Wojtowicz, *J. Power Sources* **1997**, *66*, 1.
[25] Y. T. Wu, C. C. Hu, *J. Electrochem. Soc.* **2004**, *151*, A2060.
[26] R. W. Pekala, F. M. Kong, *Polym. Preprints* **1989**, *30*, 221.
[27] R. W. Pekala, *J. Mater. Sci.* **1989**, *24*, 3221.